Macro and Micro mechanical in-situ characterization using synchrotron diffraction of Architectured micro-composite Duplex Stainless Steels

Hasan Naser, Frédéric de Geuser, Marc Mantel, Muriel Véron, Alexis Deschamps

Macro and Micro mechanical in-situ characterization using synchrotron diffraction of Architectured micro-composite Duplex Stainless Steels

Hasan Naser[a *], Frédéric De Geuser[a], Marc Mantel[a,b], Muriel Véron[a], Alexis Deschamps[a],

[a] Univ. Grenoble Alpes, CNRS, Grenoble INP, SIMaP, F-38000 Grenoble, France
[b] Ugitech Research Center, Avenue Paul Girod, 73403 Ugine Cedex, France
[*] Current affiliation: Univ. Grenoble Alpes, CEA, LETI, DCOS, LIFT, F-38000 Grenoble, France

Abstract

The mechanical behavior of micro-composites Duplex Stainless steels (DSS) produced by Accumulative re-Bundling and Drawing (ABD) has been investigated. We evidenced a systematic increase in the yield strength, as a function of the manufacturing step, independently from the phases' volume fraction. A simple rule of mixture (ROM) successfully predicted the first generation of composites presenting a simple microstructure. However, a modified ROM taking into account the contribution of each component and its grain size could not predict the mechanical response of the composites of higher generation. An in-depth analysis is conducted to investigate the microstructure-mechanical behavior relationship and to rationalize the resultant mechanical behavior from that of each constitutive phase. For this purpose, in-situ synchrotron High Energy X-ray Diffraction measurements during uniaxial tensile experiments have been carried out to calculate the strain partitioning within each phase of the composites.

Keywords: Duplex Stainless steel, Synchrotron X-Ray Diffraction, In-situ tensile tests, Micro-composites, Micromechanics

1. Introduction

The use of Duplex Stainless Steels (DSS) for structural applications is considered as one of the most significant advances impacting the construction sector [1]. These steels show a combination of properties that make them very competitive materials not only compared to carbon steels but also to austenitic stainless steels. The mechanical and functional properties of DSS can be summarized in the following points: i) very good strength/ductility compromise; ii) interesting functional properties in particular a low thermal conductivity coefficient (<15W/mK); iii) capacity of weight saving due to their high strength compared to the austenitic stainless steels and iv) low Ni content (0-4%) making the price of DSS lower and more stable.

It has been proposed that the mechanical properties of DSS result from a complex interaction between ferrite and austenite leading to a mechanical behavior that cannot be predicted from the properties of the constituents alone [2]. Several authors [3][4] [5] have attempted to model the plastic deformation of duplex stainless steels starting from the mechanical properties of single-phase tie-line alloys.

The high strength/elongation and the deviation from the law of mixture were found to be the most important features of conventional DSS. These characteristics are usually attributed, in the literature, to several factors: i) differences in plastic behavior between the ferritic and austenitic phase [6][7]; ii) residual stress and texture effects [8]–[11]; iii) Transformation Induced Plasticity (TRIP) [12], [13]; iv) other microstructural effects such as the formation of precipitations, phases' grain size or the morphology [14]–[16].

On the other hand, the effect of the microstructure morphology on the mechanical properties has been observed not only in DSS but also in other two-phase alloys. For example, in [17] the behavior of 1080 steel with pearlitic and spheroidal microstructure was studied during low-cycle fatigue. The authors found that the micro-stresses are higher in the pearlitic condition than in the spheroidal condition, and attributed these differences to a morphology effect. Indeed, the pearlite lamellae transfer the load more effectively to the cementite phase. In more recent works, the effect of volume fraction, morphology and phase distribution in dual-phase steel has been extensively reported in [18]–[21]

Several authors used multi-scale modeling and in-situ and ex-situ experiments to analyze the different parameters cited above and in particular the load sharing and stress interaction between phases and consequently the micro stress-strain curves [22][23] [6], [12], [15]. However, this approach seems to be insufficient to explain the complex plastic interaction between the ferrite and the austenite in conventional DSS microstructures [2], [12].

Thus, one can conclude that the key to the unique properties of duplex stainless steel lies in its structure and the interaction between the phases. The work of [24], for example, showed the possibility of enhancing the mechanical properties by playing with the structure of DSS. Indeed, they designed a new DSS alloy with 1 GPa of tensile strength and 60% of ductility by reducing the austenite stability and introducing Transformation Induced Plasticity (TRIP)

effect. Therefore, providing a good understanding and a full description of the mechanical behavior of DSS may provide a significant potential for breakthrough mechanical properties and particularly improving the compromise between strength and ductility.

In the present work, we investigate the mechanical behavior of DSS wires produced by Accumulative re-Bundling and Drawing (ABD), following our previous description of this material processing [25]. We evidenced in [25] a systematic increase in the yield strength, as a function of the manufacturing step, independently from the phases' volume fraction. An in-depth analysis has been conducted here to investigate the different hypotheses and to rationalize the resultant mechanical behavior from that of each constitutive phase. For this purpose, in-situ High Energy X-Ray Diffraction (HEXRD) measurements during uniaxial tensile experiments have been carried out. The advantage of this technique lies in the ability of monitor the stress-strain partitioning thanks to its selectivity based on the crystal lattices. Thus, the mechanical behavior of each phase can be observed during the tensile test. To predict and understand the flow behavior of these composites, a comparison with a micromechanical model has been then carried out. Several studies demonstrated the performance of such models to predict the stress-partitioning of various multiphase alloys and composite such as Cu-Mo [26], Duplex stainless steel [12], [27]–[29], Ferrite-Cementite [30].

2. Materials and Methods

2.1 Materials

The Architectured Duplex Stainless Steels (ADSS) samples were prepared using the Accumulative re-Bundling and Drawing (ABD) process, described in detail in our previous work [25]. Commercial austenitic and ferritic stainless steels of grades respectively 316L AISI (UGIMA® -X 4404) and 430LNb AISI (UGIMA® 4511) provided by UGITECH, have been used in elaborating ADSS wires of diameter of 1.55 mm. Wires in both as-drawn and as-annealed (850°C for 1h) condition have been characterized. The microstructure of the examined samples is shown in Figure 1, where i represents in the ni sample the number of re-bundling operations.

2.2 Macroscopic tensile tests

A high capacity 3R-syntech testing machine from UGITECH Research Centre has been used for tensile testing at room temperature. An extensometer has been used for accurate strain measurement with a deformation rate fixed at 2.10^{-4} s^{-1}. All tensile tests have been realized on wires of 1.55 mm of diameter and 300 mm of length.

2.3 Microscopic in-situ tensile experiments using high energy synchrotron X-ray diffraction

The in-situ HEXRD experiments aimed to determine the stress distribution in the different phases of our designed composites during in-situ uniaxial tensile tests at room temperature when applying increasing strain until failure. This technique also allows assessing a potential martensitic transformation induced by plastic deformation during the tensile test.

2.3.a Experimental setup

The experiment was performed at the ID15 beamline (High Energy X-ray Scattering) of the European Synchrotron Radiation Facility ESRF in Grenoble, France.

In the optical cabin, three Laue silicon monochromatic crystals are used to select three energy levels: 30, 60 and 90 keV. In the current study, the experiments were performed at an energy of 90 keV. A flat Pixium detector with 2480 x 1910 pixels of 154 µm size was used to collect the Debye-Scherrer rings at 4 Hz acquisition rate.

The tensile machine (with load sensor of 4.4 kN) was positioned on a moving table that was translated in z direction, which allowed moving both tensile grips symmetrically with respect to the X-ray beam during the tensile tests, therefore ensuring that the illuminated volume of the sample remained at the center of the gauge length. The strain rate was fixed at 2.10^{-4} s^{-1} and wires of length 50 mm have been used in this experiment.

2.3.b Analysis of the diffraction data

i) Phase fraction evolution

After calibration, a circular integration was performed to obtain the conventional diffractograms showing the intensity (I) versus diffraction angle (2θ). These diffractograms were analyzed based on austenite and ferrite diffraction spectra using Rietveld analysis via the Fullprof software. Hence, any martensite formation during tensile tests would be observed by the change in austenite fraction.

ii) Elastic strain determination

The elastic strain for a given hkl plane (ε_{hkl}) can be expressed by the following relation:

$$\varepsilon_{hkl} = \frac{d_{hkl} - d^0_{hkl}}{d^0_{hkl}} = \frac{sin\theta^0_{hkl}}{sin\theta_{hkl}} - 1 \qquad \text{Equation 1}$$

Where d^0_{hkl} (θ^0_{hkl}) represents the interplanar distance (Bragg position) of the plane hkl before loading.

In the unstrained material, the diffraction rings are perfect concentric circles. In the deformed condition, these circles bend, forming ellipses with semi-axes oriented parallel and perpendicular to the tensile direction; the major axis (a) of the ellipse and the minor axis (b) are parallel and perpendicular to the tensile direction respectively as shown in Figure 2a. Indeed, as represented in the work of [31] the hkl planes parallel to the tensile direction correspond in fact to η=0°/180° (according to our configuration) and those perpendicular to the tensile direction correspond to 90°/270°, see Figure 2b. In the current situation, the wavelength of the high energy X-rays is small and by consequence, the Bragg angles of the corresponding planes are small in the range of 2θ=3.9°-14°. This implies that the inclination of these planes versus the tensile direction can be neglected (which would not be the case for neutron diffraction). To measure the elastic deformation from the deformation of the diffraction rings, we discretized the diffraction rings into 8 portions of 45 °, Figure 2c, and then made the azimuthal integration. The intensity of Bragg reflections I^{ph} for the phase ph was then fitted by a Lorentzian function:

$$I^{ph}(2\theta) = I_0 + \sum_{hkl} \frac{2A}{\pi} \frac{w^{hkl}}{4(2\theta - 2\theta_0^{hkl})^2 + (w^{hkl})^2}$$ Equation 2

Where:

I_0 the baseline offset
A total area under the curve from the baseline
$2\theta_0^{hkl}$ center of the peak hkl
w^{hkl} full width of the peak hkl at half height

Figure 3 shows the diffractograms of the composites in the loading direction after radial integration, initially before the tensile test with a preload of 10 MPa to set up the sample and to ensure its alignment. This acquisition was taken as the initial diffraction state. Six Bragg peaks are accessible for the γ phase, namely (111), (200), (311), (222) and (400). The most intense families of planes are (111) and (200). Regarding the α phase, 5 Bragg peaks are accessible, namely (110), (200), (211), (220) and (310) of which the family of planes (110) and (211) are the most intense. **Error! Reference source not found.** shows the respective average proportions of austenite and ferrite quantified by HEXRD measurements.

3. Results and discussion

The mechanical behavior of the ADSS composites is studied following two approaches: the first one is a macroscopic investigation relying on the comparison with the mechanical behavior of individual wires of both phases 316L and 430LNb and the resultant composites microstructure. The second approach is microscopic, consisting in studying the behavior of the composites individual phases using the HEXRD data.

3.1 Macroscopic mechanical behavior

3.1.a Composite n1 annealed at 1050°C

The stress-strain curve of the n1 composite is compared in Figure 4 with that of wires of the commercial grades 316L and 430LNb of diameter 1.55mm, identical to those used in the manufacturing of n1 composite and subjected to similar thermomechanical conditions. The austenitic and ferritic wires have been drawn from 2.2 mm and 1.8mm down to 1.55 mm of diameter, for ferrite and austenite respectively. Both wires have been then annealed at 1050°C for 10 minutes in a vacuum vertical furnace. In these annealing conditions, the 430LNb steel becomes significantly softer than the 316L steel.

To predict the mechanical behavior of n1 composite, a simple law of mixture can be applied. Indeed, if the flow stress σ is modeled according to an isostrain rule of mixtures (ROM), the flow stress of the composite σ_c can be written as a function of the flow stress of the two constituents and their volume fraction as following:

$$\sigma_c(\varepsilon) = V_{316L}\sigma_{316L}(\varepsilon) + V_{430LNb}\sigma_{430LNb}(\varepsilon)$$ Equation 3

Where ε is the strain, σ_c, σ_{316L} and σ_{430LNb} are the flow stress of the composite and of the 316L and 430LNb wires, respectively. V_{316L} and V_{430LNb} are the volume fractions of the constituting phases (316L and 430LNb respectively) present in composite n1. The volume fraction of the austenite and the ferrite has been estimated by image analysis to be 45% and 55%, respectively.

As shown in Figure 4, a good approximation is obtained between experimental results and modeling with the simple law of mixture expressed in equation 3, despite the slight difference in the yield strength, namely 263 MPa in experiment against 230 MPa predicted by ROM. The applicability of the ROM is expected for this composite since no significant changes in terms of microstructure, have occurred between the individual wires and those of the n1 composite. Indeed, if we compare the average grain size of ferrite inside the n1 composite (measured from EBSD maps) and that of the individual wires (calculated by interception method on optical micrographs) we find a similar average grain size ≈ 55µm. On the other hand, the average grain size of the individual wire of 316L is slightly larger (60µm) than that inside the n1 composite (50µm), which could explain the slightly larger yield strength in the composite.

3.1.b Composite n(i>1) annealed 850°C

Unlike the n1 composite, the tensile behavior of n2, n3 and n4 composites was examined after annealing at a lower temperature (i.e. 1h at 850°C with a heating rate of 70°C/h), to avoid excessive interdiffusion between the two constituents. The composites' tensile curves, shown in Figure 5, are thus compared with those of individual wires of 316L and 430LNb heat-treated in this case at 850°C for a duration of 1h with a heating rate of 70°C/h.

Although the volume fraction of each phase varies for each composite, one can notice the increase of the flow stress at each step. Indeed, the n2 and n4 composites have the same volume fraction of ferrite (76%vol), however, the flow stress of n4 composite is significantly higher than that of n2. A similar trend is observed in n3 and n5 composite (43% of austenite). The evolution of yield strength, tensile strength and uniform elongation are summarized in Figure 6. One can notice the strong increase of yield strength between n2 and n3. However, the increase in yield strength becomes relatively slow between n4 and n5.

Compared to the individual wires of 316L and 430LNb, it is interesting to notice that none of the composites' flow stress is situated between that of 316L and 430LNb wires. Indeed, the flow stress of n2 composite, with 77% of ferrite, fits perfectly with the flow stress curve of 430LNb wire up to 10% strain beyond which the work hardening of n2 composite starts to increase. On the other hand, the flow stress of n3 (43 % of γ), n4 (24% of γ) and n5 (43% of γ) exceed that of 316L wire.

Figure 7 shows the stress-strain curves for composites (n2,n4) and (n1,n3), these pairs having respectively the same initial fraction of ferrite and austenite. The results evidence a systematic increase in flow stress for composites n (i>1) for a given fraction of austenite phase as a function of the manufacturing step. Three hypotheses could explain this systematic increase: i) Strain-induced martensite transformation; ii) contribution of thermal martensite; iii) phase / grain size effect.

The first hypothesis can be ruled out since the austenite phase present inside the composites (316L) is stable with respect to plastic deformation at room temperature [32]. In Figure 7, a quantitative analysis of phase evolution during the tensile tests has been realized and shows indeed that the austenitic phase inside all composites is stable, *i.e.* no transformation to martensite has occurred. In addition, these results show that the stability of the austenitic phase is not significantly disrupted by the changes in the chemical composition of 316L due to interdiffusion of solute elements during the annealing steps [25].

The presence of the thermal martensite in ADSS has already been evidenced and discussed in our previous work [25] and its contribution to the mechanical behavior could be significant in composites n (i>1), since the fraction of martensite increases together with the interfacial area between ferrite and austenite, and with the extent of interdiffusion.

As shown in Figure 8 for the n4 composite, the presence of this martensite appears as a thin layer of very small grains at the boundaries of the ferritic regions. The estimation of the volume fraction of martensite formed within the vicinity of the interface γ/α increases to reach 1.6%, 5.1, 5.6 and 6% in composites n2, n3, n4 and n5 respectively. These fractions are calculated by assuming that the martensite is formed within a constant layer within the vicinity of ferrite/austenite interface and inside 316L phase. The thickness of this layer was taken to be the maximum observed by EBSD and TEM [25], namely 3µm.

The variation of grain size within the ferritic region of the composite could also partly explain the systematic increase of the mechanical properties. A sample processed by several steps of ADB possesses a spatially heterogeneous microstructure, because of the different history that the different generations of wires and tubes have been subjected to. For a given ni sample (subjected to i steps of ADB), one can differentiate the regions corresponding to the different generations when the materials have been introduced in the process ($j \leq i$). Using local and global EBSD maps, the grain size of each component in n3, n4 and n5 were measured, and are represented in Figure 9. One can notice two features:

- Within the same composite, the grain size for a given phase is smaller in the old generations than in the new ones. In other words, a decrease of grain size is noticed for a given phase moving from the external tube towards the core of the wire.
- For a given generation and phase, one can notice a systematic decrease of grain size when i (number of composite) increases.

In order to examine the possible influence of the grain size on the yield strength of the composites, Hall-Petch relation and rule of mixture can be used. The Hall-Petch relationship for both austenite and ferrite phases has been constructed using individual wires of 316L and 430LNb. These wires were subjected to different thermo-mechanical operations as shown in Table 2.

Figure 10 shows the relation between the yield strength measured by tensile testing as a function of the inverse of the square root of grain size for individual wires 316L and 430LNb.

The Hall Petch relationship for both bulk wires was then expressed as follows (in MPa):

$$\sigma_y^{316L} = 201.4 + \frac{351.3}{\sqrt{d}} \quad \text{Equation 4}$$

$$\sigma_y^{430LNb} = 181.5 + \frac{305}{\sqrt{d}} \quad \text{Equation 5}$$

Hence, the yield strength of the composite n(i) σ_c can be calculated by taking into account the contribution of each generation. The ROM can then be written as follows:

$$\sigma_c = \sum_{j=1} V_j^{316L} \sigma_j^{316L} + \sum_{j=1} V_j^{430LNb} \sigma_j^{430LNb} \quad \text{Equation 6}$$

Where V_j^{ph} and σ_j^{ph} are the volume fraction and the yield strength of the phase *ph* issued from generation *j* respectively. Table 3 compares these predictions to the experimental values. A significant difference between the calculated and the experimental yield strengths is observed.

This difference between the ROM and the experiments can be attributed to the fact that the Hall Petch relationship is derived from individual bulk wires, which are not representative for the austenitic and ferritic phase in the composites, especially at large ni numbers because of extensive inter-diffusion between the phases that cause changes in their mechanical properties. In order to understand further the micro-composites' mechanical behavior, we will now carry out a local analysis of the behavior of each phase during the tensile test.

3.2 In-situ tensile tests

3.2.a Peak selection

When performing in-situ measurements with X-ray diffraction, it has been established that the suitable {hkl} planes for measuring the stress within one phase are those whose elastic strain have a linear response with the applied macroscopic stress (in the elastic regime). Indeed, such linearity means that these {hkl} planes are less affected by intergranular interactions, allowing therefore properly converting a measured lattice strain into equivalent stress by Hooke's law [33].

Figure 11 shows the evolution of elastic strains for different {hkl} planes of the austenite phase in composites n2 and n3 with macroscopic applied stress. A strong anisotropic behavior and non-linear behavior of all {hkl} planes is revealed in the elastic part, meaning that none of the {hkl} reflections represent the macroscopic stress behavior [34], [35]. Therefore, it is necessary to take into account the contribution of each {hkl} plane reflection to produce a macroscopic equivalent strain $\overline{\varepsilon_{ph}}$. Daymond's model (METHOD B) [33] is used in this study to calculate the equivalent strain by calculating the weighting of each measured peak with the following equations:

$$\overline{\varepsilon_{ph}} = \frac{\sum_{hkl} \alpha_{hkl}^{ph} \varepsilon_{hkl}^{ph}}{\sum_{hkl} \alpha_{hkl}^{ph}} \quad \text{Equation 7}$$

$$\alpha_{hkl}^{ph} = \frac{E_{hkl}^{ph}}{u_{hkl}^2 d_{hkl}^{ph} pA(\lambda) F_{hkl}^2 sin^2\theta} \quad \text{Equation 8}$$

Where α_{hkl}^{ph} is the weighting function of the individual diffraction peak {hkl} of phase (ph), ε_{hkl}^{ph} is the strain obtained in analyzing the {hkl} reflection of the phase (ph), E_{hkl}^{ph} is the diffraction elastic constant for {hkl} diffraction peak of the phase (ph), u_{hkl} is the uncertainty of individual {hkl} reflection measurement, p is the polarization factor, A represents an absorption term, F is the structure factor.

This model is suitable for our study since we have shown in previous work [25] that the texture of an ADSS depends on the composite type and varies as a function of generation for a given phase.

The determination of the weighting factors in equation 6 requires the knowledge of the plane-specific Young's moduli for the two phases E_{hkl}^{ph}. To measure these elastic constants, we used samples of composites containing ≈43%γ (n3 and n5) and those containing ≈76% α (n2 and n4) in the as-drawn state, which show very high yield strength and thus an extensive elastic regime. Figure 12 shows the relationships between applied stress and lattice strains for the as-drawn n3 composite, and Table 4 shows the measured E_{hkl} in this work compared with those measured in the work of [35] and [36] for FCC and BCC phase respectively. Due to its weak intensity in as-drawn state, $(E_{220})_{\gamma}$ could not be measured. The measured values are in very good agreement with those from the literature.

3.2.b Averaged stress calculation

In order to assess the load sharing between both phases, average phase stresses rather than average lattice strains are required. The composite's stress can then be calculated using mixture and Hooke's law as follows:

$$\sigma_c = V_\gamma \sigma_\gamma + V_\alpha \sigma_\alpha = V_\gamma E_\gamma \overline{\varepsilon_\gamma} + V_\alpha E_\alpha \overline{\varepsilon_\alpha} \qquad \text{Equation 9}$$

Where V_γ and V_α; are the phase volume fractions. The bulk Young moduli, E_γ and E_α, of the commercial 316L AISI (UGIMA® -X 4404) and 430LNb AISI (UGIMA® 4511) are 196 GPa and 220 GPa, respectively. Combining Equation 5 with 7, the composite stress can be rewritten:

$$\sigma_c = V_\gamma E_\gamma \left(\frac{\sum_{hkl} \alpha_{hkl}^{\gamma} \varepsilon_{hkl}^{\gamma}}{\sum_{hkl} \alpha_{hkl}^{\gamma}} \right) + V_\alpha E_\alpha \left(\frac{\sum_{hkl} \alpha_{hkl}^{\alpha} \varepsilon_{hkl}^{\alpha}}{\sum_{hkl} \alpha_{hkl}^{\alpha}} \right) \qquad \text{Equation 10}$$

Figure 13 compares the calculated stress strain curves with the experimental macroscopic tensile tests of the investigated composites n2, n3, n4 and n5 after annealing. Interesting features can be observed in this figure:

- Very good agreement between the averaged calculated stress using Equation 4 and the macroscopic tensile curve is obtained for composites n2, n3 and n4.

- The calculated stress curve of composite n5 (43%vol of austenite) shows a significant decrease of its slope starting from 7% of true strain.

Several parameters can explain these features. First, one possible explanation of the slope change of n5 composite could be the contribution of a third phase in the strengthening process. As demonstrated previously, no martensitic transformation occurred during the tensile test. Nevertheless, all composites contain already a martensitic phase inherited from the previous steps. Therefore, the presence of this martensite may partly explain the change in slope in the n5 composites. Under this hypothesis, the larger slope change in the n5 composite could originate from its containing more accumulated martensite than other composites. Moreover, the architecture perturbation in composite n5 originated from extensive intediffusion, as evidenced in [25], causes microstructural changes in terms of grain size and chemical composition of the austenitic phase issued from older generation.

Secondly, in this kind of experiment, the diffraction spectra of each phase are representative of the average response. However, the mechanical behavior of an individual phase in the composite is also dependent of the behavior of the phases issued from each generation of the composite, as it was discussed previously and demonstrated in our previous work [25]. Indeed, a variation of the grain size and the texture as a function of the generation within the same phase has been revealed. This was attributed to the thermomechanical history undergone by each component.

Figure 14 summarizes the calculated separate stress evolution of the austenite and ferrite phase of all composites as a function of the macroscopic true strain. It shows the systematic increase of the calculated stresses for both phases as a function of the composite n, which is consistent with our discussion on the influence of the grain size within the phases. This data also evidences the stronger strain hardening rate in the austenite phase within the composites, and conversely the higher yield strength in the ferrite phase.

Thus, Daymond's model used in this work to describe the macroscopic mechanical behavior starting from local mechanical response gives a very good approximation. Thanks to this model, we can conclude that for a filamentary duplex stainless steel, the increase of the mechanical properties results, indeed, from the microstructure of each phase and generation within the same phase rather than a complex interaction between the two phases and their distribution.

4. Conclusion

- A systematic increase in composites' flow stress as a function of the manufacturing step independently from the phase volume fraction has been observed.

- A simple rule of mixture (ROM) from the constituent's materials stress-strain curves successfully predicts the n1 composite's flow stress.

- The flow stress of composites n>1 shows a high deviation from the simple ROM. A modified ROM taking into account the contribution of each component and its grain size failed in the prediction of the mechanical behavior. Thus, the limit of the macroscopic approach has been drawn.

- Lattice strains of both phases BCC and FCC were successfully measured by synchrotron X-ray diffraction for ADSS composites n>1 during tensile tests carried out on the as-drawn and as-annealed state.

- The strain partition of each phase has been calculated by taking into account the contribution of each hkl plane

- The calculated macroscopic stress-strain starting from local mechanical response gave a very good approximation for composite n2, n3 and n4. On the other hand, the model evidenced the possible influence of the martensite induced upon cooling and the microstructure perturbation due to the extensive interdiffusion on the mechanical behavior of composites n5.

Acknowledgments

This work was performed within the framework of the Center of Excellence of Multifunctional Architectured Materials "CEMAM" n°AN-10-LABX-44-01 funded by the "Investments for The Future Program". F. Moser at Ugitech is gratefully acknowledged for help with the drawing process. Dr. N. Meyer is thanked for fruitful dicussions. Dr. F. Robaut is thanked for help with EBSD observations. Dr. A. Lechartier is thanked for help during HEXRD experiments. The technical staff of ID15 beamline at ESRF is gratefully acknowledged for support during the experiments.

Data availability

The raw/processed data required to reproduce these findings cannot be shared at this time due to legal or ethical reasons.

References

[1] N. R. Baddoo, « Stainless steel in construction: A review of research, applications, challenges and opportunities », *Journal of Constructional Steel Research*, vol. 64, n° 11, p. 1199- 1206, 2008, doi: 10.1016/j.jcsr.2008.07.011.

[2] J. Nilsson et G. Chai, « The physical metallurgy of duplex stainless steels », *Proceedings Duplex Stainless Steel*, vol. 97.5, p. 73- 82, 1997.

[3] M. Nyström et B. Karlson, « Plastic deformation of duplex stainless steels with different amounts of ferrite », in *Fourth International Conference DUPLEX STAINLESS STEELS, Glasgow, Scotland 13-16 November*, 1994.
[4] K. Cho et J. Gurland, « The Law of Mixtures Applied to the Plastic Deformation of Two-Phase Alloys of Coarse Microstructures », *Metallurgical and Materials Transactions A*, vol. 19A, n° August, p. 1988- 2040, 1988, doi: 10.1007/BF02645206.
[5] T. S. Byun et I. S. Kim, « Stress and strain partition in elastic and plastic deformation of two phase alloys », *Journal of Materials Science*, vol. 26, n° 14, p. 3917- 3925, 1991, doi: 10.1007/BF01184992.
[6] A. Baczmański *et al.*, « Elastoplastic deformation and damage process in duplex stainless steels studied using synchrotron and neutron diffractions in comparison with a self-consistent model », *International Journal of Plasticity*, vol. 81, p. 102–122, 2016.
[7] J. Johansson, M. Oden, et X.-H. Zeng, « Evolution of the residual stress state in a duplex stainless steel during loading », *Acta materialia*, vol. 47, n° 9, p. 2669–2684, 1999.
[8] R. Dakhlaoui, A. Baczmański, C. Braham, S. Wroński, K. Wierzbanowski, et E. C. Oliver, « Effect of residual stresses on individual phase mechanical properties of austeno-ferritic duplex stainless steel », *Acta Materialia*, vol. 54, n° 19, p. 5027–5039, 2006.
[9] N. Jia, R. L. Peng, Y. D. Wang, S. Johansson, et P. K. Liaw, « Micromechanical behavior and texture evolution of duplex stainless steel studied by neutron diffraction and self-consistent modeling », *Acta Materialia*, vol. 56, n° 4, p. 782–793, 2008.
[10] N. Jia *et al.*, « Interactions between the phase stress and the grain-orientation-dependent stress in duplex stainless steel during deformation », *Acta Materialia*, vol. 54, n° 15, p. 3907–3916, 2006.
[11] D. Chalapathi, P. V. Sivaprasad, et A. K. Kanjarla, « Role of deformation twinning and second phase on the texture evolution in a duplex stainless steel during cold rolling: Experimental and modelling study », *Materials Science and Engineering: A*, p. 139155, 2020.
[12] Y. Tian, S. Lin, J. P. Ko, U. Lienert, A. Borgenstam, et P. Hedström, « Micromechanics and microstructure evolution during in situ uniaxial tensile loading of TRIP-assisted duplex stainless steels », *Materials Science and Engineering: A*, vol. 734, p. 281–290, 2018.
[13] A. Lechartier *et al.*, « Deformation behavior of lean duplex stainless steels with strain induced martensitic transformation: Role of deformation mechanisms, alloy chemistry and predeformation », *Materialia*, vol. 5, p. 100190, 2019.
[14] M. Okayasu et D. Ishida, « Effect of Microstructural Characteristics on Mechanical Properties of Austenitic, Ferritic, and γ-α Duplex Stainless Steels », *Metallurgical and Materials Transactions A*, vol. 50, n° 3, p. 1380–1388, 2019.
[15] C. U. Jeong, Y.-U. Heo, J. Y. Choi, W. Woo, et S.-H. Choi, « A study on the micromechanical behaviors of duplex stainless steel under uniaxial tension using ex-situ experimentation and the crystal plasticity finite element method », *International Journal of Plasticity*, vol. 75, p. 22–38, 2015.
[16] P. Hedström, T.-S. Han, U. Lienert, J. Almer, et M. Odén, « Load partitioning between single bulk grains in a two-phase duplex stainless steel during tensile loading », *Acta Materialia*, vol. 58, n° 2, p. 734–744, 2010.
[17] R. A. Winholtz et J. B. Cohen, « Load sharing of the phases in 1080 steel during low-cycle fatigue », *Metallurgical Transactions A*, vol. 23, n° 1, p. 341- 354, janv. 1992, doi: 10.1007/BF02660876.

[18] Y. Ososkov, D. S. Wilkinson, M. Jain, et T. Simpson, « In-situ measurement of local strain partitioning in a commercial dual-phase steel », *International journal of materials research*, vol. 98, n° 8, p. 664–673, 2007.
[19] J.-Y. Kang *et al.*, « Phase analysis of steels by grain-averaged EBSD functions », *ISIJ international*, vol. 51, n° 1, p. 130–136, 2011.
[20] S.-H. Choi, E.-Y. Kim, W. Woo, S. H. Han, et J. H. Kwak, « The effect of crystallographic orientation on the micromechanical deformation and failure behaviors of DP980 steel during uniaxial tension », *International Journal of Plasticity*, vol. 45, p. 85–102, 2013.
[21] S.-H. Choi, E.-Y. Kim, et S. I. Kim, « The micromechanical deformation behaviors of hot-rolled 590FB steel during hole-expansion test », *International Journal of Plasticity*, vol. 58, p. 184–200, 2014.
[22] G. C. Chai et R. Lillbacka, « Damage and crack initiation behavior of duplex stainless steel during cyclic loading », in *Key Engineering Materials*, 2006, vol. 324, p. 1117- 1122.
[23] N. Jia *et al.*, « Interactions between the phase stress and the grain-orientation-dependent stress in duplex stainless steel during deformation », *Acta Materialia*, vol. 54, n° 15, p. 3907- 3916, 2006.
[24] C. Herrera, D. Ponge, et D. Raabe, « Design of a novel Mn-based 1GPa duplex stainless TRIP steel with 60% ductility by a reduction of austenite stability », *Acta Materialia*, vol. 59, n° 11, p. 4653- 4664, 2011, doi: 10.1016/j.actamat.2011.04.011.
[25] H. Naser, A. Deschamps, M. Mantel, et M. Véron, « Architectured duplex stainless steels micro-composite: Elaboration and microstructure characterization », *Materials & Design*, vol. 145, p. 156- 167, 2018, doi: https://doi.org/10.1016/j.matdes.2018.02.069.
[26] A. Wanner et D. C. Dunand, « Synchrotron X-ray study of bulk lattice strains in externally loaded Cu-Mo composites », *Metallurgical and Materials Transactions A*, vol. 31, n° 11, p. 2949- 2962, 2000, doi: 10.1007/BF02830344.
[27] R. Dakhlaoui, C. Braham, et A. Baczmański, « Mechanical properties of phases in austeno-ferritic duplex stainless steel—Surface stresses studied by X-ray diffraction », *Materials Science and Engineering: A*, vol. 444, n° 1, p. 6- 17, 2007, doi: https://doi.org/10.1016/j.msea.2006.06.074.
[28] Y. Zhao *et al.*, « Stress distribution correlated with damage in duplex stainless steel studied by synchrotron diffraction during plastic necking », *Materials & Design*, vol. 113, p. 157- 168, 2017, doi: https://doi.org/10.1016/j.matdes.2016.10.014.
[29] N. Tsuchida, T. Kawahata, E. Ishimaru, A. Takahashi, H. Suzuki, et T. Shobu, « Static Tensile Deformation Behavior of a Lean Duplex Stainless Steel Studied by In Situ Neutron Diffraction and Synchrotron Radiation White X-rays », *ISIJ International*, vol. 53, n° 7, p. 1260- 1267, 2013, doi: 10.2355/isijinternational.53.1260.
[30] V. Taupin, R. Pesci, S. Berbenni, S. Berveiller, R. Ouahab, et O. Bouaziz, « Lattice strain measurements using synchrotron diffraction to calibrate a micromechanical modeling in a ferrite–cementite steel », *Materials Science and Engineering: A*, vol. 561, p. 67- 77, 2013, doi: 10.1016/j.msea.2012.10.086.
[31] M. L. Young, J. D. Almer, M. R. Daymond, D. R. Haeffner, et D. C. Dunand, « Load partitioning between ferrite and cementite during elasto-plastic deformation of an ultrahigh-carbon steel », *Acta Materialia*, vol. 55, n° 6, p. 1999- 2011, 2007, doi: 10.1016/j.actamat.2006.11.004.
[32] K. H. Lo, C. H. Shek, et J. K. L. Lai, « Recent developments in stainless steels », *Materials Science and Engineering: R: Reports*, vol. 65, n° 4- 6, p. 39- 104, 2009, doi: 10.1016/j.mser.2009.03.001.

[33] M. R. Daymond, « The determination of a continuum mechanics equivalent elastic strain from the analysis of multiple diffraction peaks », *Journal of applied physics*, vol. 96, n° 8, p. 4263- 4272, 2004.
[34] M. R. Daymond, C. Hartig, et H. Mecking, « Interphase and intergranular stress generation in composites exhibiting plasticity in both phases », *Acta Materialia*, vol. 53, n° 9, p. 2805- 2813, 2005, doi: 10.1016/j.actamat.2005.02.041.
[35] B. Clausen, T. Lorentzen, et T. Leffers, « Self-consistent modelling of the plastic deformation of f.c.c. polycrystals and its implications for diffraction measurements of internal stresses », *Acta Materialia*, vol. 46, n° 9, p. 3087- 3098, 1998, doi: 10.1016/S1359-6454(98)00014-7.
[36] M. R. Daymond et H. G. Priesmeyer, « Elastoplastic deformation of ferritic steel and cementite studied by neutron diffraction and self-consistent modelling », *Acta Materialia*, vol. 50, n° 6, p. 1613- 1626, 2002, doi: https://doi.org/10.1016/S1359-6454(02)00026-5.

Figure(s)

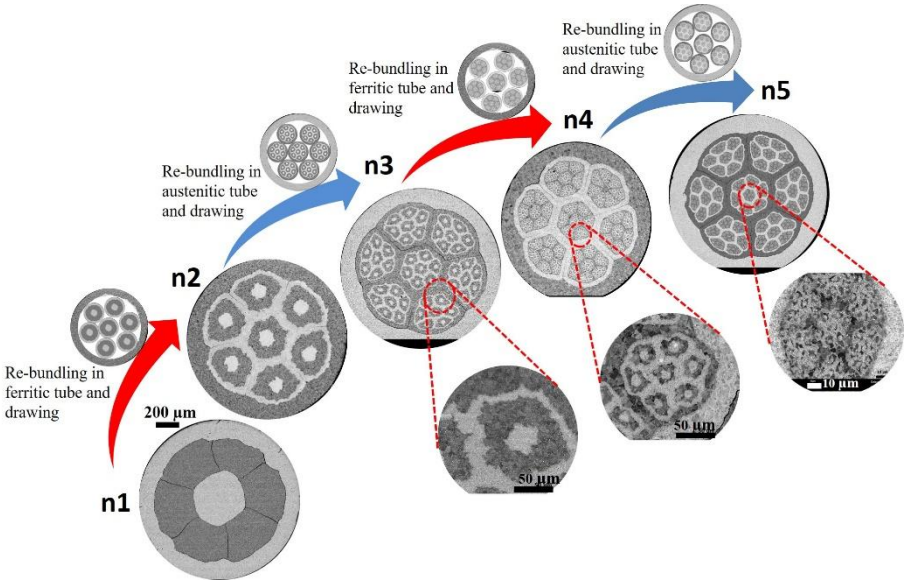

Figure 1: SEM images of the cross-sections of the composites n1, n2, n3, n4 and n5

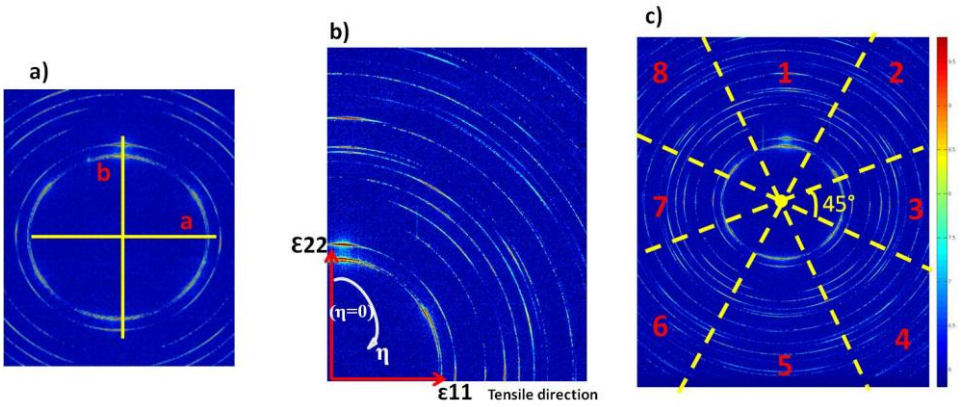

Figure 2: Example of HEXRD diagram after deformation ; a) elliptic shape of the diffraction patterns after deformation ; b) quadrant of the diffraction pattern showing the tensile direction ; c) discretization of the diffraction pattern

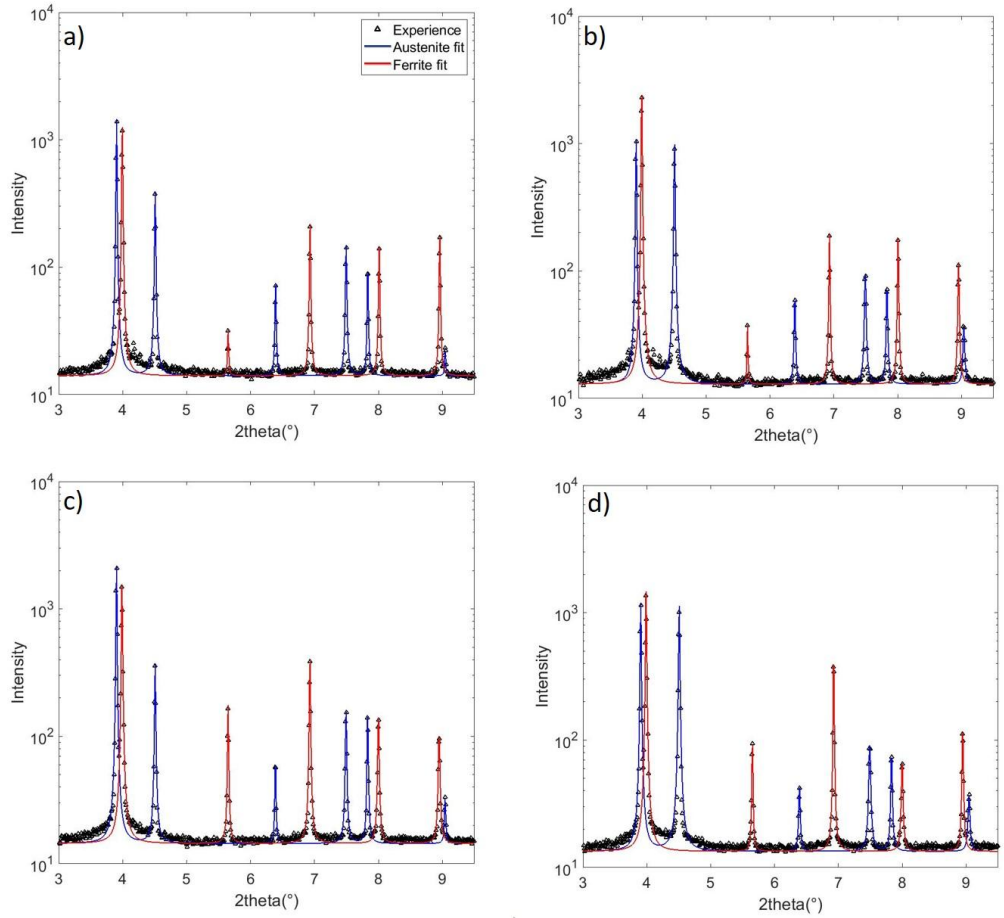

Figure 3: 2θ diffractograms representing austenite (blue) and ferrite (red) peaks fitted with Lorentzian function at initial state (before straining) for composites n2 (a), n3 (b), n4 (c) and n5 (d) after annealing at 850°C for 1hour

	n2	n3	n4	n5
Austenite	23%	43%	24%	43%
Ferrite	77%	57%	76%	57%

Table 1: Austenite and ferrite volume fractions for the different composites, determined from the analysis of the HEXRD data

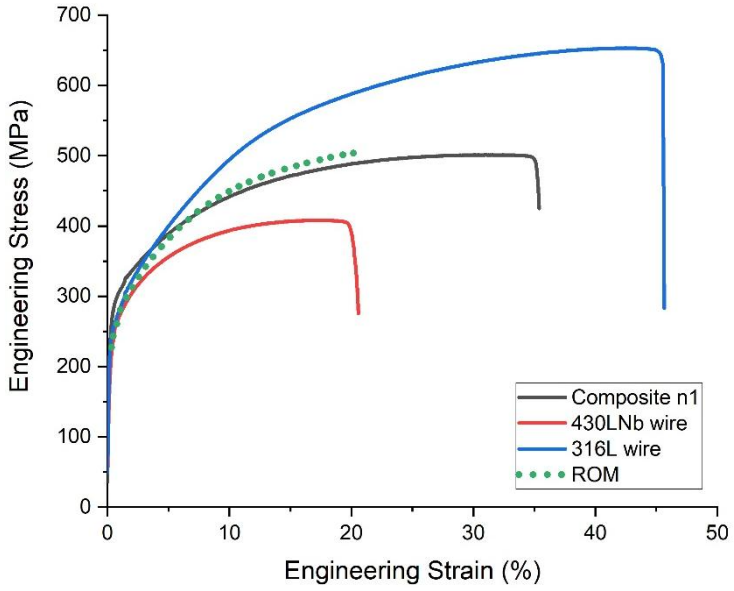

Figure 1: Mechanical response of n1 composite after annealing for 10 minutes at 1050°C compared with wires of the base materials, and prediction by the rule of mixtures (ROM).

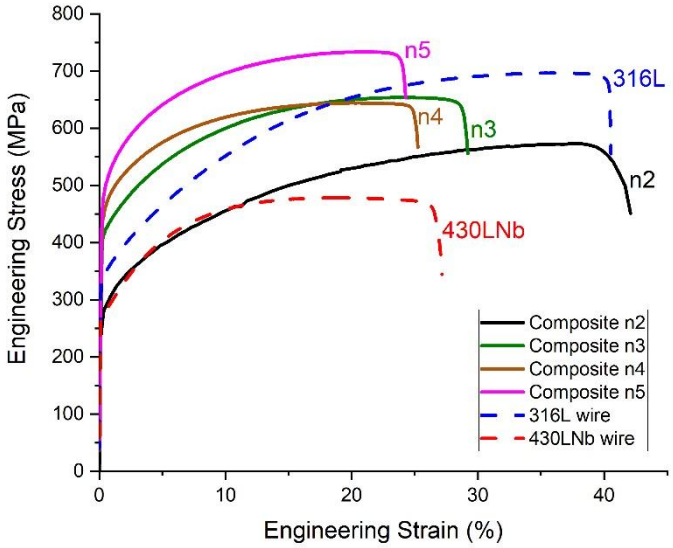

Figure 5: Mechanical response of composites n(i>1) annealed at 850°C compared with wires of the base materials

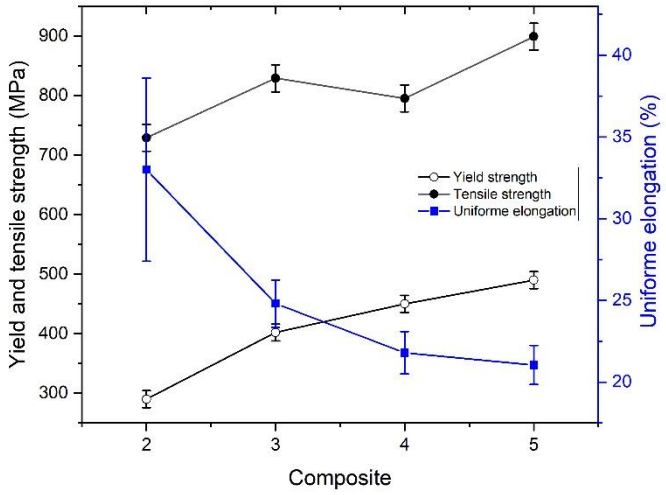

Figure 6: Evolution of yield strength, tensile strength and uniform elongation, as a function of the generation number n of the composite

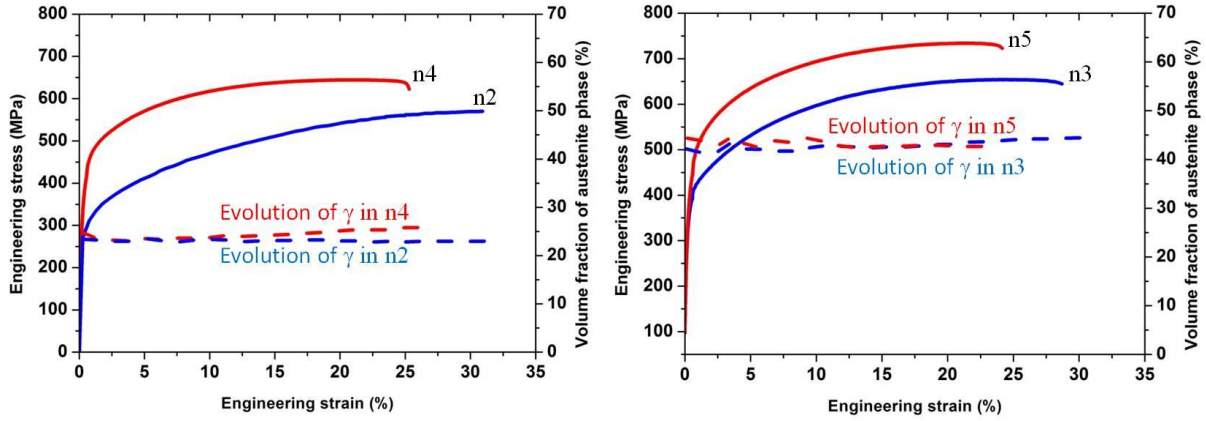

Figure 7: In-situ tensile tests for n2; n4, n3 and n5 composites (continuous lines), and austenite fractions (dashed lines) as a function of strain, determined by HEXRD analysis

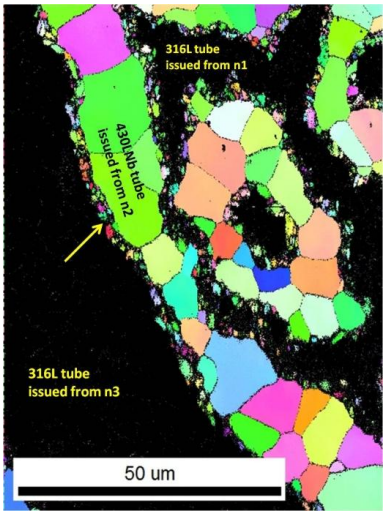

Figure 8: EBSD map of the microstructure of composite n4: the colored region is the ferritic phase and the black region is the austenitic phase; the arrow indicates the small grains between ferritic and austenite zones.

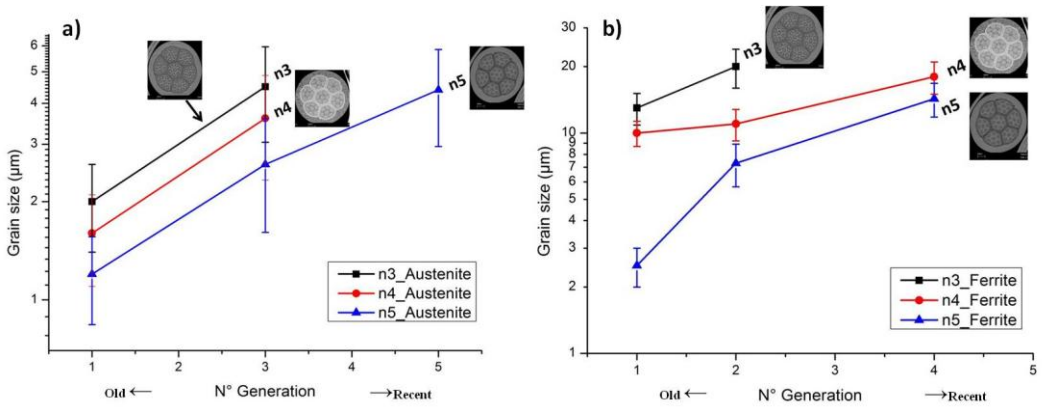

Figure 9: Grain size evolution of each component (generation) for composite n3, n4 and n5 after annealing at 850°C for 1 hour: a) austenite, b) ferrite

316L						
Wire	Deformation	Heat-treatments	Yield strength (MPa)	Micro-hardness (HV)	average grain diameter d (µm)	$1/\sqrt{d}$
1	Section reduction from Φ=5.5mm down to 1.5mm	850@1min	470	227	1.8	0.745
2		850@5min	440	215	2.1	0.690
3		850@1h	410	212	2.6	0.620
4		950@1h	312	162	16.7	0.245
5	Section reduction from Φ=1.8mm down to 1.5mm	1050@10min	233	150	50	0.141
430LNb						
1	Section reduction from Φ=5.5mm down to 1.5mm	850@1h	266	162	11.6	0.294
2	Section reduction from Φ=2.2.mm down to 1.5mm	900@10 min	293	165	8	0.354
3		1050@10min	224	150	55	0.134

Table 2: Experimental data of 316L and 430LNb wires used for determining the Hall-Petch relationship

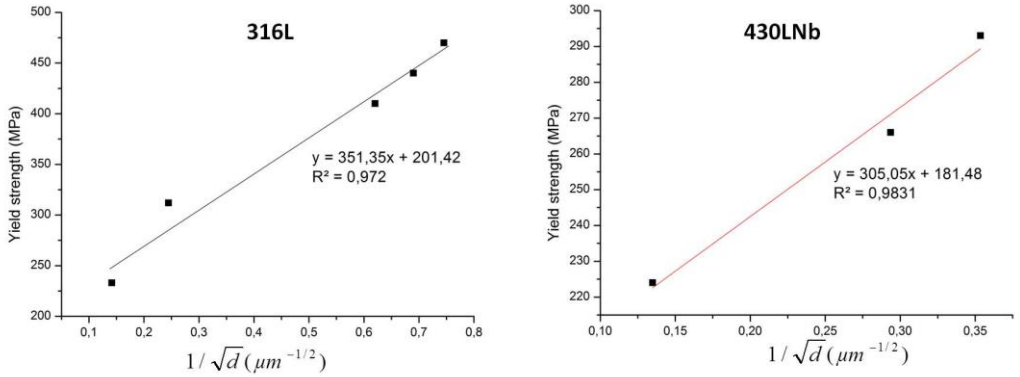

Figure 10: Yield strength as a function of inverse square root of grain size for 316 and 430LNb

composite	σ_y Calculated ROM (MPa)	σ_y Experimental (MPa)	Error
n3	318	402	20%
n4	298.4	450	33%

Table 3: Comparison between ROM and experimental yield strengths for composites n3 and n4

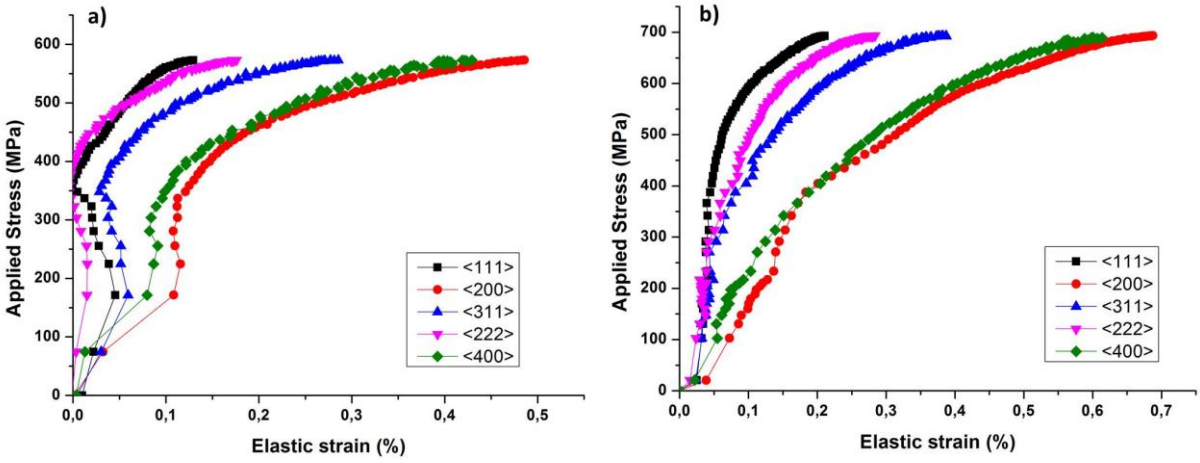

Figure 11: Change in elastic strain of austenite lattice planes during a uniaxial tensile test of composite a) n2 (25%austenite); b) n3 (45% austenite)

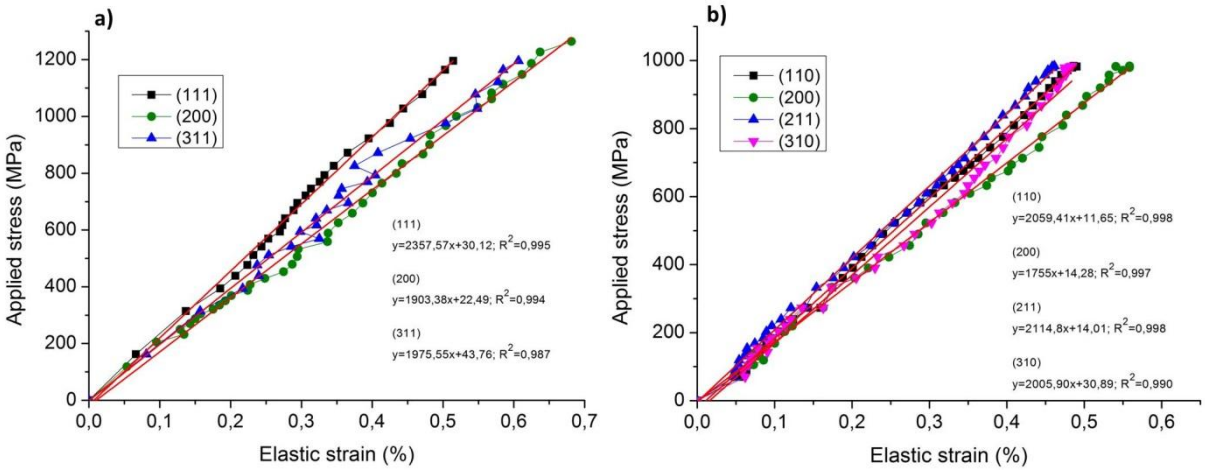

Figure 12: Applied stress as a function of lattice strain in the elastic regime for composites n in the as-drawn state for (a) austenite and (b) ferrite.

	Austenite			**Ferrite**	
hkl	$E_{hkl}\ (GPa)$ measured in this work	$E_{hkl}\ (GPa)$ [35]	**hkl**	$E_{hkl}\ (GPa)$ measured in this work	$E_{hkl}\ (GPa)$ [36]
111	235.7	246.2	**110**	205	225
200	184.6	149.8	**200**	175.5	170
220	-	212	**211**	211.4	215
311	197.5	183.2	**310**	196	185

Table 4: Measured and calculated elastic constants E_{hkl} for the BCC and FCC phases for each composite

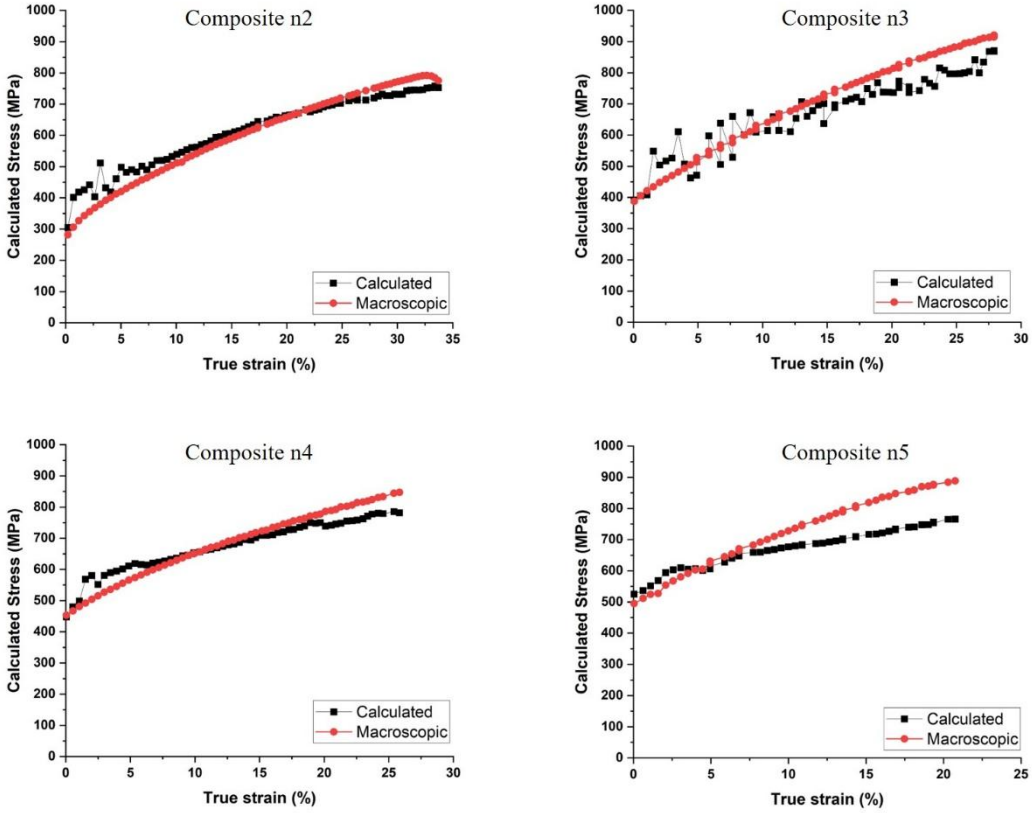

Figure 13: True stress vs. applied true strain calculated from synchrotron X-ray diffraction data for composites n2, n3, n4 and n5 in annealed state

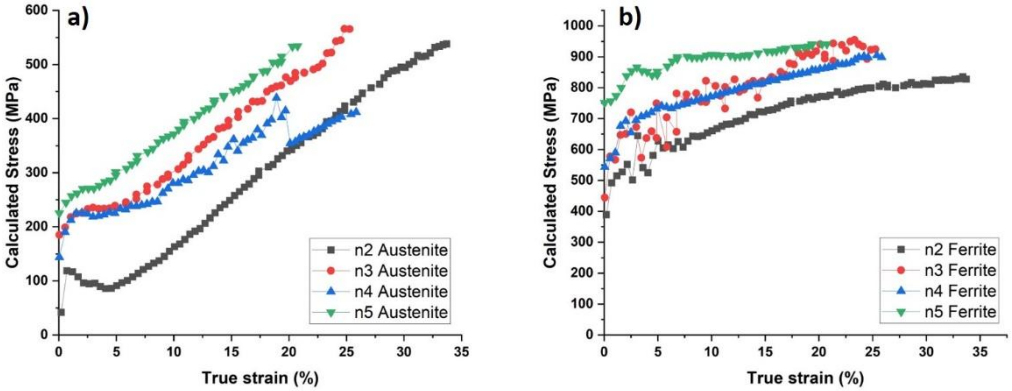

Figure 14: Calculated stress *vs* applied true strain of (a) austenite phase and (b) ferrite phase for each composites n2, n3, n4 and n5